# Microwave-Vortex-Beam Generation Based on Spoof-Plasmon Ring Resonators

Zhen Liao[ORCID],[1,2,3] Jia Nan Zhou,[1] Guo Qing Luo,[1,*] Meng Wang,[3] Shi Sun,[3] Tao Zhou,[1]
Hui Feng Ma[ORCID],[3,†] Tie Jun Cui,[3] and Yongmin Liu[2,‡]

[1]*Key Laboratory of RF Circuits & System of Ministry of Education, Hangzhou Dianzi University, Xiasha High Education Park, Hangzhou 310018, China*
[2]*Department of Mechanical and Industrial Engineering, Northeastern University, Boston, Massachusetts 02115, USA*
[3]*State Key Laboratory of Millimeter Waves, Southeast University, Nanjing 210096, China*

Vortex beams carrying orbital angular momentum (OAM) have recently attracted great interest due to their capability for providing a new method to increase the communication channels in wireless communications. It is expected that the unbounded eigenstates of OAM can bring a large number of channels to enhance the transmission capacity. Here, we propose an effective strategy to generate vortex beams by using spoof surface plasmon polaritons (SSPPs) in the microwave region. A periodically modulated SSPP ring resonator is applied to convert near-field SSPP waves into radiating a vector vortex beam. The emitted beam can possess different OAM modes at different frequencies through rational design. In addition, circularly polarized vortex beams are demonstrated. Both numerical simulations and experimental characterizations confirm the theoretical predictions. Owing to the deep subwavelength characteristic of SSPP, the proposed device can be readily integrated into miniaturized circuits and systems. We anticipate that our design will enable a wide range of applications for future wireless communication technologies.

## I. INTRODUCTION

Vortex beams, which carry orbital angular momentum (OAM), are manifested by a helical phase front and an azimuthal component of the wave vector [1]. Optical vortex beams have recently attracted considerable interest, because of their promising application perspectives, including optical microscopy [2], superresolution imaging [3,4], and optical tweezers [5]. After a series of profound researches in optics, the basic physical properties and characteristics of OAM have been translated to microwave and millimeter waves [6–12]. In contrast to the spin angular momentum (SAM) that can only take two orthogonal states, the OAM has unbounded eigenstates. Therefore, in principle, OAM beams can offer many channels and tremendously enhance communication capacity without increasing the bandwidth in wireless communication systems [8]. To date, various approaches have been developed to generate OAM beams, including spiral parabolic antennas [13], antenna arrays [9,14], metasurfaces [15–18], leaky-wave antennas [10,19,20], and ring resonators [21].

These methods, however, have several limitations. For instance, it is difficult to implement multiplexing and demultiplexing using spiral parabolic antennas for beam generation. Although it is easy to produce electromagnetic vortex with the circular antenna array, the exact controlled phase-shift feeding network is necessary, which increases the cost and the complexity of the system. Meanwhile, microscale ring resonators have been used to generate light beams carrying OAM. The design idea is to make the ring resonator surrounded by scatters, which have a specific phase delay with respect to the neighboring scatter, resulting in a helical phase front [22–24].

In recent years, the concept of spoof surface plasmon polaritons (SSPPs) has been developed by using structured metals, such as one-dimensional grooves or two-dimensional hole arrays drilled into metals. These structured metal surfaces support highly confined surface electromagnetic (EM) waves at low frequencies. Their properties are very similar to those of conventional surface plasmon polaritons (SPPs) at optical frequencies. As we know, SPPs start to lose the strong-field confinement when the frequency is below the mid-infrared. The reason is that metals behave as perfect electric conductors at low frequencies. However, by structuring metals to form one-dimensional or two-dimensional metallic waveguides and operating at the frequency below the cutoff

---

*luoguoqing@hdu.edu.cn
†hfma@seu.edu.cn
‡y.liu@northeastern.edu

frequency of these waveguide, EM fields exponentially decay along the surface normal direction. Such a feature imitates conventional SPPs, while the dispersion characteristics and spatial confinement of the SSPP can be readily controlled by geometrical means [25–27].

SSPPs have been used to produce compact microwave components in wireless communication systems in the microwave and millimeter wave region. For instance, Su *et al.* fabricated a well-designed deep-subwavelength metaparticle, generating near-field electromagnetic vortex modes at the microwave frequency [28]. In addition, SSPP-based vortex-beam emitters have started to attract attention. Not only can these SSPP-based vortex-beam emitters be easily integrated to communication systems, but also have the potential to solve the challenge of transmission data rate in wireless communications. For example, Yin *et al.* proposed a looped SSPP waveguide surrounded by a series of circular patches to generate vortex beam. Each patch works as a radiation unit, while gives rise to the phase shifts required by the vortex beam [29]. The SSPP waves travel on the waveguide and couple to the patches, while the patches radiate waves. However, it is difficult to implement multiplexing and demultiplexing because this device only generates single-type vortex beam at each frequency. The double-layer configuration used in the device can result in the OAM order inconsistencies in upward and downward directions. In addition, the double-layer layout and affiliated patches increase the complexity of the proposed structure, which are not favorable for the design and fabrication of system.

In this paper, we propose and demonstrate an alternative route to emit the vortex beams with multiplexing and demultiplexing capabilities, by utilizing a SSPP ring resonator based on a planar corrugated microstrip line. The SSPP ring resonator is manufactured by folding a straight SSPP leaky-wave antenna (LWA) into a circular loop. In this way, the radiated beam transforms into a cylindrical vector vortex (CVV) beam. The radiated CVV beam can carry OAM, which is demonstrated by theoretical analysis and numerical simulations. The electric field scanning pattern is measured. The measured results agree very well with the simulations. We show that the different OAM modes are generated at different frequencies without any changes in the structure. Furthermore, we present numerical and experimental far-field results to demonstrate that our device can emit two kinds of circular-polarized vortices with different topological charges. Our work provides an effective way to convert SSPP waves to OAM-carrying spatial waves, which can easily be integrated into wireless communications systems and integrated circuits operating in the low frequency regions. The demonstrated multiplexing and demultiplexing of the OAM-carried waves substantially advances the practical applications of OAM-based wireless communication.

## II. RESULTS

### A. Structure and design

Recently, corrugated metal structures were proposed and investigated to support SSPPs confined in a subwavelength scale, while periodically modulated SSPP waveguide LWA composed of nonuniform corrugated metallic strip can convert traveling SSPPs to radiating waves [30–32]. Figure 1(a) shows the top view of the SSPP waveguide LWA. The substrate with metal ground is F4B, with a relative permittivity of 2.5 and loss tangent of 0.003. The thickness of the dielectric substrate is 3 mm. The geometry of the SSPP waveguide is designed as $a = 2$ mm, $d = 4$ mm, and $p = 20$ mm. In order to efficiently convert SSPP to radiating waves, the surface impedance of the waveguide is modulated by changing the depths of metal grooves in one period. The groove depths are $h_1$, $h_2$, $h_3$, $h_4$, and $h_5$, respectively.

In this particular design, the triangular-modulated surface impedance in one period can be written as

$$Z_s(x) = \begin{cases} jX_s\left(1 + \frac{2M}{p}x - \frac{M}{2}\right) & \text{if } 0 \leq x \leq \frac{p}{2} \\ jX_s\left(1 - \frac{2M}{p}x + \frac{3M}{2}\right) & \text{if } \frac{p}{2} \leq x \leq p \end{cases}, \quad (1)$$

where $X_s$ is the average surface reactance, and $M$ is the modulation factor. The $-$first-order harmonic, which is the first spatial harmonic, is usually used to generate the leaky-wave radiation [33]. The phase constant $\beta_x$ of the first radiating harmonic mode can be calculated as

$$\beta_x = k_{-1} = k_x - \frac{2\pi}{p}, \quad (2)$$

where $k_x$ is the wavenumber of the SSPP wave along the propagating direction in the waveguide. The angle of the radiation beam is given by $\alpha = \sin^{-1}(\beta_x/k_0)$, where $k_0$ is the vacuum wavenumber. Here, we set $\alpha = 0$ to observe the leaky waves propagating along the normal direction (i.e., along the $z$ axis) at 8 GHz, which means $\beta_x = 0$ and $k_x = 2\pi/p$. Furthermore, the average surface reactance of the corrugated metallic strip can be calculated to be $X_s = 598 \, \Omega$ through

$$Z = \eta_0\sqrt{1 - (k_x/k_0)^2}, \quad (3)$$

where $\eta_0$ is the wave impedance in free space. In our design, we choose $M = 0.5$ to get an efficient radiation. Solving Eq. (3), we can find that the surface impedance of the triangularly modulated SSPP waveguide LWA in one period equals 448, 598, 748, 598, and 448 $\Omega$, respectively, at the location of the five metallic grooves.

In order to find the geometry of the grooves to match the desired surface impedance, the dispersion curves of the
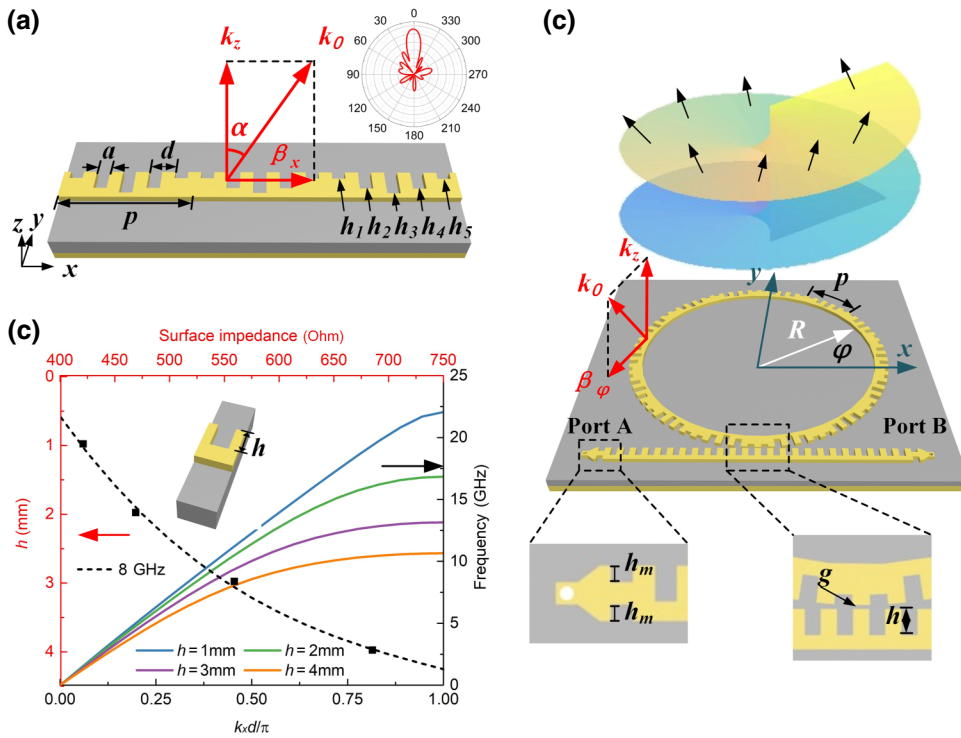
FIG. 1. (a) Schematic of triangularly modulated SSPP waveguide LWA using corrugated microstrip line. The inset shows the far-field radiation pattern. (b) The dispersion curves and the surface impedances of the unit. (c) Illustration of the SSPP ring resonator that is coupled to an access waveguide for wave input.

unit cell with different groove depths are numerically simulated, and plotted in Fig. 1(b) with solid lines. It is apparent that the SSPP exhibit different propagating constants $k_x$ when the groove depth $h$ varies. The surface impedances of the corrugated conductors with groove depths $h = 1$, 2, 3, 4 mm at 8 GHz are calculated by Eq. (3). Then the data are fitted by the dashed line in Fig. 1(b). We can observe that the surface impedance ranges from the 425 to 750 Ω as the groove depth changes from 0.4 to 4.2 mm, which can be used to design the depth of the subwavelength corrugated metal structure. Consequently, the groove depths can be determined through the relationship between surface impedance and groove depth $h$ at 8 GHz. The groove depths thus are defined as $h_1 = h_5 = 1.56$ mm, $h_2 = h_4 = 3.41$ mm, $h_3 = 4.24$ mm.

The inset of Fig. 1(a) represents the simulated far-field, two-dimensional (2D) radiation pattern of this design, which shows that the periodically modulated corrugated structure can radiate a beam along the normal direction at 8 GHz. Please note that the single-strip corrugated metallic structure without ground can also be used as LWA. However, the major lobe of its radiation pattern does not point along the $z$ axis, owing to the asymmetric structure. Therefore, we use SSPP structures along with a metallic ground plate to ensure the upward radiation. On the other hand, the SSPP waves have different wave numbers at different frequencies, so the radiation angle can be steered by changing the frequency. In the proposed design, the wave front of the radiating beam is tilted except at 8 GHz. When the frequency is below 8 GHz, the main lobe of radiation is backward, while the radiation beam is forward

at the frequency above 8 GHz. If the waveguide LWA is designed with circular shape, the tilted phase front of the radiating beam is twisted into a spiral about the direction perpendicular to the structure progressively.

Subsequently, we bend the designed straight SSPP waveguide LWA into a ring, whose circumference is $n$ times the length of the modulated period $p$. Here we set $n = 14$, as shown in Fig. 1(c). In this way, the SSPP waves are guided around the ring, leading to whispering-gallery modes (WGMs). The resonant condition should satisfy the equation [34]

$$2\pi R = m\lambda/n_{\text{eff}}, \qquad (4)$$

where $m$ denotes the mode number of the ring resonator, $n_{\text{eff}}$ is the effective index of the SSPP mode, which can be described as $n_{\text{eff}} = k_\varphi/k_0$, and $\lambda$ stands for the wavelength in free space. In order to couple the wave into the ring resonator, a linear SSPP waveguide with groove depth $h = 3.24$ mm is placed near the ring resonator. The distance between the ring resonator and the waveguide is $g = 0.5$ mm. The linear SSPP waveguide is fed from the back by coaxial connector. At each terminal (ports A and B) of the linear SSPP waveguide, a notch groove with $h_m = 1.5$ mm is employed for impedance matching between the corrugated metallic strip and the coaxial connector (see the enlarged diagram of port A).

Because the radius $R$ is much bigger than the groove width of the ring, the wavenumber $k_\varphi$ in the azimuthal direction is nearly equal to the wavenumber $k_x$ of the original straight SSPP waveguide LWA. Meanwhile, the

periodically modulated ring resonator can also emit the first radiating harmonic beam. Here the wavenumber of the $-$first-order harmonic mode in azimuthal direction is

$$k_{-1,\varphi} = k_\varphi - \frac{2\pi}{p}. \tag{5}$$

Substituting Eq. (4) into Eq. (5), we can obtain the azimuthal propagation constant (i.e., phase shift per unit azimuthal angle) of the radiating beam

$$\beta_\varphi = k_{-1,\varphi} R = \left( k_\varphi - \frac{2\pi}{p} \right) R = \frac{2\pi R n_{\text{eff}}}{\lambda} - \frac{2\pi R}{p} = m - n \tag{6}$$

at the resonance frequency, where $m$ is the azimuthal order of the resonance, and $n$ is the number of modulated periods around the resonator.

Note that the radiated wave is a rotationally symmetric beam with respect to the $z$ axis. Therefore, the beam should be a CVV beam. As mentioned in Ref. [30], the polarization of the radiating beam is parallel with the SSPP propagation direction. Thus, the CVV beam emerging from the ring is predominantly azimuthally polarized in our particular design. When port A is excited, the traveling WGMs propagate along the anticlockwise direction, the $-$first-order harmonic radiation field can be written as the following form:

$$E_\varphi = E_0(r,z) e^{-j\beta_\varphi \varphi} \hat{\varphi}, \tag{7}$$

where $E_0(r, z)$ is the azimuthal amplitude of the far field and $\varphi$ is the azimuthal angle. This radiating wave is a vector vortex beam with spatial inhomogeneous polarization distribution. Following the discussion in Ref. [35], the phase of the CVV is characterized by $e^{-jl\varphi}$, where $l$ is

the Pancharatnam topological charge. Moreover, the vector vortices have intriguing spiral wavefronts that carry OAM. The topological Pancharatnam charge should correspond with the OAM vortices [36]. Therefore, in our periodically modulated SSPP ring resonator, OAM carried by the radiating wave is $l = \beta_\varphi = m - n$ at the resonance frequencies.

### B. Simulations and measurements

In order to validate our design, we perform numerical simulations by CST Microwave Studio, a commercial electromagnetic solver. The simulated S parameters, that is, $S_{11}$ as reflection and $S_{21}$ as transmission, are plotted as solid lines in Fig. 2(a). One can see that the transmission spectrum has several dips in the frequency range from 6.5 to 9.5 GHz, resulting from the resonances. It should be noted that the reflection coefficient at 8 GHz is bigger than other frequencies, which is due to the open stopband (OSB) at broadside radiation [37–40]. We fabricate the porotype using printed-circuit-board technology for measurements. The materials and geometries in experiments are the same as those in simulations. The experimental results are plotted as dashed lines in Fig. 2(a), which show very good agreement with the simulations. To explain the phenomena, we simulate $E_z$-field distributions in the $x$-$y$ plane 3 mm above the structures at these resonance frequencies. From Figs. 2(b)–2(h), we can see that the near-field patterns correspond to WGMs of the ring resonator, with mode number $m$ ranging from 11 to 17. Following the aforementioned discussion, the wavenumber of the traveling WGMs $k_\varphi$ should be equal to $2\pi/p$ at 8 GHz. Therefore, the number of optical periods $m = 14$ in the resonator circumference at 8 GHz. Here the experimental and simulated results match well with the theoretical prediction, verifying the accuracy of the design.
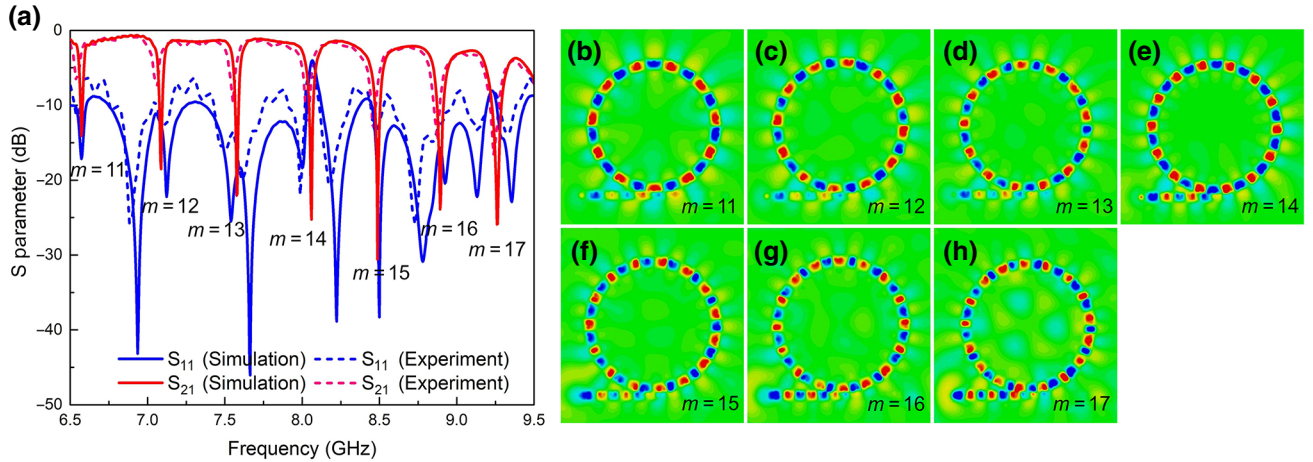


FIG. 2. (a) Simulated and measured S parameters of the proposed structure. (b)–(h) indicate the near field at 6.53, 7.06, 7.55, 8, 8.45, 8.87, and 9.23 GHz, corresponding to mode number $m = 11, 12, 13, 14, 15, 16, 17$.
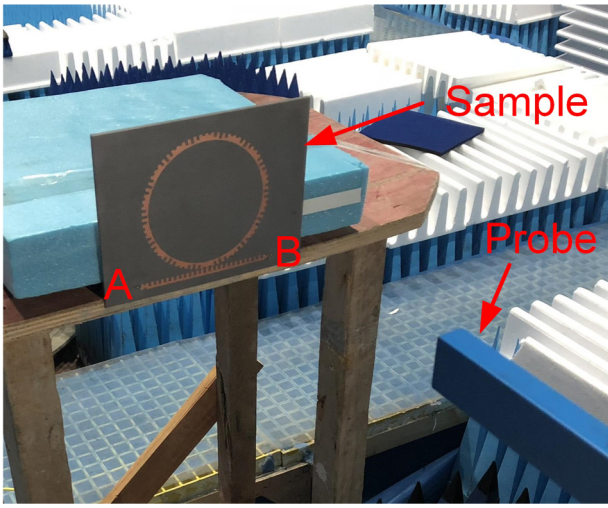
FIG. 3.    Experimental setup in an anechoic chamber.

In order to further verify that the radiating wave carry OAM, we perform electric field scanning measurement using the setup shown in Fig. 3. An open-end waveguide is adopted as the probe. The waveguide is connected to the Agilent VNA. The fabricated sample is fixed, in which port A of the access waveguide is connected to the VNA and port B is connected with $50\,\Omega$ matching impedance. The distance between the structure and probe is set at 400 mm (ten times of the wavelength at the central frequency 8 GHz). The probe can move along the horizontal and vertical directions step by step controlled by a 2D stage, and record the electric field data. During the measurement, the field distribution with horizontal polarization is first scanned, then we rotate the probe by 90 ° to record the field distribution with vertical polarization. By the vector coordinate transforms, the normalized phase distributions of azimuthal component can be plotted. The comparisons between the simulated and measured normalized phase distributions at 6.53, 7.06, 7.55, 8, 8.45, 8.87, and 9.23 GHz are presented in Figs. 4(a) and 4(b). As we discuss, the azimuthal order of the resonance is $m = 14$ at 8 GHz. Therefore, the OAM carried by the emitting beam is predicted by $l = m - n = 0$ at 8 GHz, which has no Pancharatnam topological charge. From Fig. 4, it is evident that this beam exhibits no spiral phase and no OAM at 8 GHz as the theory predicts. For other frequencies, phase gradient along the azimuth direction are obtained, in which the phase changes by $-6\pi$, $-4\pi$, $-2\pi$, $2\pi$, $4\pi$, $6\pi$ upon one full circle around the center of the vortex at 6.53, 7.06, 7.55, 8.45, 8.87, and 9.23 GHz, respectively. The phase is continuous everywhere except near the center, presenting a phase singularity at the beam axis. The results confirm that the emitted field from our system carries OAM of $l = -3$, $-2$, $-1$, 0, 1, 2, and 3 at each of the resonance frequencies, respectively, consistent with the theoretical analysis. The excellent agreement can be further observed from the

comparison between measurement and full-wave simulation. The results demonstrate that the proposed method of emitting vortex beams carrying OAM modes by SSPP ring resonator is effective. Moreover, the variable OAM can be generated by tuning the azimuthal order $m$ on the resonance and the number of modulated periods $n$ around the resonator.

Given the knowledge above, when port A is fed and port B is matched, the anticlockwise-traveling WGMs appear in the ring and emit the beam carrying OAM of $l$. Because of the symmetry of this device, the clockwise-traveling WGM distributed fields can be excited by coupling wave into port B. In this case, the device radiates the helix beam with the OAM modes of $-l$ with respect to clockwise-traveling WGMs at the same resonance frequencies. The radiated wave of our design will carry $+l$ or $-l$ OAM mode according to the feeding option of the input port A or B for the access waveguide. It means that this device is an intrinsic dual OMA mode antenna without extra multiplexing devices. More interestingly, based on the proposed structure, multiple SSPP rings can easily be integrated into one system by linear array or multiple concentric rings, which are coupled to the access waveguide. With a delicate design, more than two OAM modes' multiplexing and demultiplexing can be conveniently achieved.

### C. Scalar vortex beams

Furthermore, we show that the CVV beam can be considered as a combination of left-hand circularly polarized (LHCP) and right-hand circularly polarized (RHCP) radiated OAM beams given by [23,41–43]

$$E_\varphi = E_0(r,z)e^{-jl\varphi}\hat{\varphi} = -\frac{j}{2}\big[-E_0(\hat{x} - j\hat{y})e^{-j(l-1)\varphi}$$
$$+E_0(\hat{x} + j\hat{y})e^{-j(l+1)\varphi}\big]. \qquad (8)$$

Therefore, the far-field radiation from the ring resonator can be decomposed into two scalar vortices, which are LHCP beams with topological charge of $l+1$ and RHCP beams with $l-1$. Note that the circular polarization is defined from the point of view of the source. Two different polarization OAM states exist at the same frequencies. By the cooperation with the input, four OAM modes' ($l-1$, $-l-1$ for RHCP and $l+1$, $-l+1$ for LHCP) multiplexing can be conveniently achieved. This feature could result in more channels and communication capacities compared with traditional OAM antennas.

To illustrate the OAM-carrying vortex behavior, Fig. 5 presents the simulated LHCP and RHCP far-field radiation pattern and phase distribution in a three-dimensional plot at 6.53, 7.06, 7.55, 8, 8.45, 8.87, and 9.23 GHz, respectively. For convenience and clear identification of the far-field characteristics, all the patterns at each frequency are normalized to their maximal intensity. As expected,
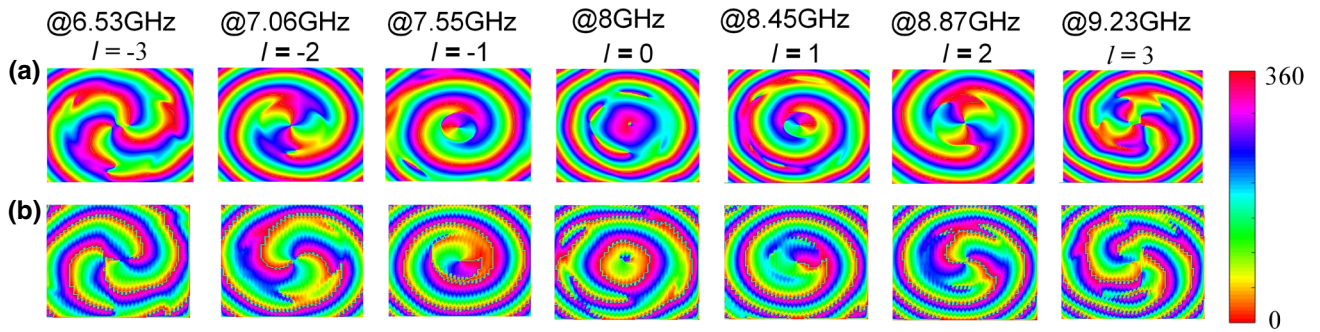
FIG. 4.   (a) Simulated and (b) measured phase distribution of emitted wave with the azimuthal polarization at the resonance frequencies.

the LHCP far field [Fig. 5(a)] have spiral phase change equal to $(l+1) \times 2\pi$ at resonances. Figure 5(b) shows that the LHCP far-field pattern is a pencil-like beam at 7.55 GHz and an amplitude null in the central region at other resonance frequencies. Thus, the LHCP beams correspond to topological charge of $-2, -1, 0, 1, 2, 3, 4$ at the seven resonance frequencies. On the other hand, the RHCP phase patterns [see Fig. 5(c)] have spiral arms equal to $l-1$ and the handedness determine the sign of the topological charge, which reveal that the emitting RHCP beams exhibited OAM modes of $-4, -3, -2, -1, 0, 1, 2$ at resonances.

For the case when the topological charge is nonzero, the far-field radiation patterns of the RHCP beam form a donut shape, as shown in Fig. 5(d). When the topological charge is 0 at 8.45 GHz, the emitted RHCP beam does not possess a net OAM value as predicted.

Figures 6(a) and 6(b) plot the LHCP and RHCP normalized 2D far-field radiation patterns at the seven resonance frequencies. The simulated and measured far-field patterns show very good agreement. For LHCP beam at 7.55 GHz, an ordinary beam is obtained since the mode number is zero, as predicted before. Hollow radiation patterns are
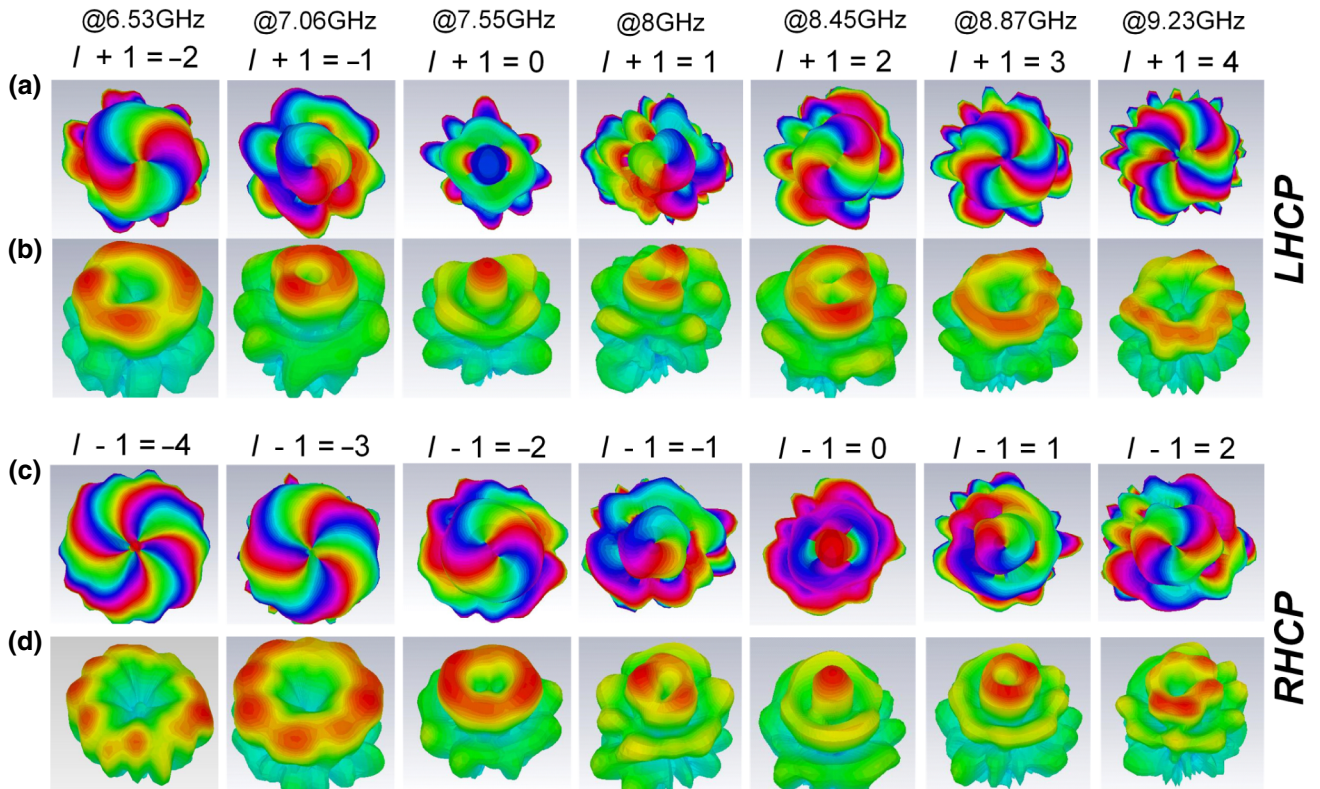


FIG. 5.   Numerically calculated far-field (a) phase patterns and (b) radiation patterns of the emitted LHCP beams at 6.53, 7.06, 7.55, 8, 8.45, 8.87, and 9.23 GHz. Numerically calculated far-field (c) phase patterns and (d) radiation patterns of the emitted LHCP beams at resonances frequencies.
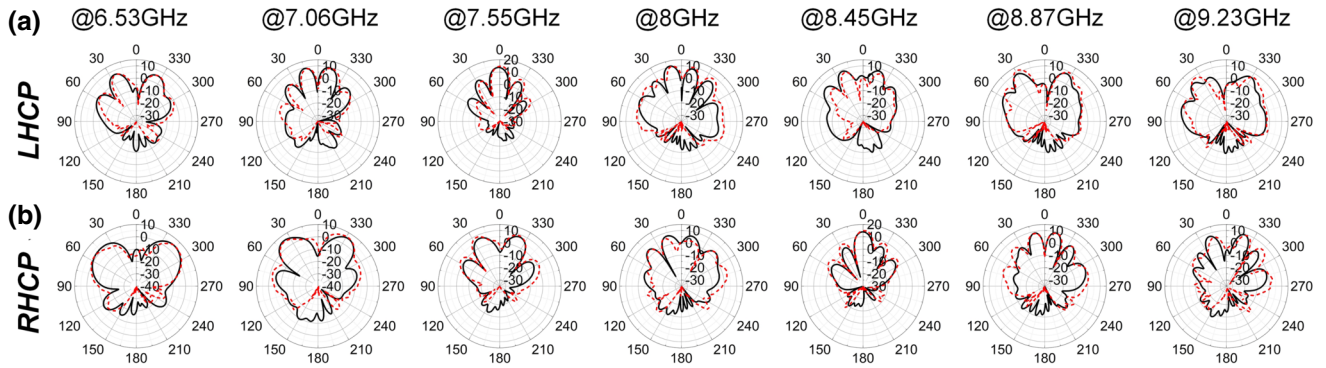
**(a)**



**(b)**



FIG. 6.    Measured and simulated far-field 2D radiation patterns of (a) LHCP and (b) RHCP. The solid line indicates the simulated results, while dashed lines are measured results.

achieved at other frequencies as expected. The RHCP far-field radiation pattern exhibit a pencil-like beam at 8.45 GHz, whereas there is an angle between the two main lobes at other frequencies. Both simulated and measured results of LHCP and RHCP far-field patterns prove that the previous analysis is accurate, and our design can be used to emit circular-polarized vortices.

## III. CONCLUSION

We propose and demonstrate an efficient approach to convert SSPP waves to vortex beams by SSPP ring resonators. Simulations and experimental characterizations confirm the theoretical prediction that the emitted CVV beams from the present configuration carry well-defined OAM. These vortex beams with different OAM modes are observed at different frequencies. The mode numbers of $l = -3, -2, -1, 0, 1, 2, 3$ appear at 6.53, 7.06, 7.55, 8, 8.45, 8.87, and 9.23 GHz respectively. Moreover, it is confirmed with simulations and measurements that this device can be used to emit LHCP and RHCP vortex beams simultaneously. This structure can possess more flexible OAM modes by adjusting the azimuthal order of the resonance and the number of modulated periods around the resonator. Our results enable many potential applications, including but not limited to the multiplexing and demultiplexing of the OAM radio waves in wireless communication and detecting the OAM of CVV and circular-polarized vortices.

## ACKNOWLEDGMENTS

[1] L. Allen, M. W. Beijersbergen, R. J. C. Spreeuw, and J. P. Woerdman, Orbital angular momentum of light and the transformation of Laguerre-Gaussian laser modes, Phys. Rev. A **45**, 8185 (1992).

[2] S. Fürhapter, A. Jesacher, S. Bernet, and M. Ritsch-Marte, Spiral interferometry, Opt. Lett., OL **30**, 1953 (2005).

[3] V. Skarka, N. B. Aleksić, and V. I. Berezhiani, Evolution of singular optical pulses towards vortex solitons and filamentation in air, Phys. Lett. A **319**, 317 (2003).

[4] S. Bretschneider, C. Eggeling, and S. W. Hell, Breaking the Diffraction Barrier in Fluorescence Microscopy by Optical Shelving, Phys. Rev. Lett. **98**, 218103 (2007).

[5] S. Sato, M. Ishigure, and H. Inaba, Optical trapping and rotational manipulation of microscopic particles and biological cells using higher-order mode Nd:YAG laser beams, Electron. Lett. **27**, 1831 (1991).

[6] B. Thidé, H. Then, J. Sjöholm, K. Palmer, J. Bergman, T. D. Carozzi, Ya. N. Istomin, N. H. Ibragimov, and R. Khamitova, Utilization of Photon Orbital Angular Momentum in the Low-Frequency Radio Domain, Phys. Rev. Lett. **99**, 087701 (2007).

[7] S. M. Mohammadi, L. K. S. Daldorff, J. E. S. Bergman, R. L. Karlsson, B. Thide, K. Forozesh, T. D. Carozzi, and B. Isham, Orbital angular momentum in radio—A system study, IEEE Trans. Antennas Propag. **58**, 565 (2010).

[8] F. Tamburini, E. Mari, A. Sponselli, B. Thidé, A. Bianchini, and F. Romanato, Encoding many channels on the same frequency through radio vorticity: First experimental test, New J. Phys. **14**, 033001 (2012).

[9] A. Tennant and B. Allen, Generation of OAM radio waves using circular time-switched array antenna, Electron. Lett. **48**, 1365 (2012).

[10] S. Zheng, X. Hui, X. Jin, H. Chi, and X. Zhang, Transmission characteristics of a twisted radio wave based on circular traveling-wave antenna, IEEE Trans. Antennas Propag. **63**, 1530 (2015).

[11] L. Cheng, W. Hong, and Z.-C. Hao, Generation of electromagnetic waves with arbitrary orbital angular momentum modes, Sci. Rep. **4**, 4814 (2014).

[12] C. Pfeiffer and A. Grbic, Controlling Vector Bessel Beams with Metasurfaces, Phys. Rev. Appl. **2**, 044012 (2014).

[13] A. Sa, P. Br, S. Gopinath, S. Bs, T. W. Sj, and S. S. Ga, Simulation of the S-band photon vorticity modulation scheme, Am. J. Electromagnetics Appl. **1**, 38 (2013).

[14] Q. Bai, A. Tennant, and B. Allen, Experimental circular phased array for generating OAM radio beams, Electron. Lett. **50**, 1414 (2014).

[15] Y. Yuan, X. Ding, K. Zhang, and Q. Wu, Planar efficient metasurface for vortex beam generating and converging in microwave region, IEEE Trans. Magn. **53**, 1 (2017).

[16] H. Xu, H. Liu, X. Ling, Y. Sun, and F. Yuan, Broadband vortex beam generation using multimode pancharatnam–berry metasurface, IEEE Trans. Antennas Propag. **65**, 7378 (2017).

[17] E. Karimi, S. A. Schulz, I. De Leon, H. Qassim, J. Upham, and R. W. Boyd, Generating optical orbital angular momentum at visible wavelengths using a plasmonic metasurface, Light: Sci. Appl. **3**, e167 (2014).

[18] J. Yang, C. Zhang, H. Ma, W. Yuan, L. Yang, J. Ke, M. Chen, A. Mahmoud, Q. Cheng, and T. Cui, Tailoring polarization states of multiple beams that carry different topological charges of orbital angular momentums, Opt Express **26**, 31664 (2018).

[19] A. Al-Bassam, M. A. Salem, and C. Caloz, in 2014 IEEE Antennas and Propagation Society International Symposium (APSURSI) (2014), pp. 1792–1793.

[20] Z. Zhang, S. Zheng, X. Jin, H. Chi, and X. Zhang, Generation of plane spiral OAM waves using traveling-wave circular slot antenna, IEEE Antennas Wirel. Propagation Lett. **16**, 8 (2017).

[21] X. Hui, S. Zheng, Y. Chen, Y. Hu, X. Jin, H. Chi, and X. Zhang, Multiplexed millimeter wave communication with dual orbital angular momentum (OAM) mode antennas, Sci. Rep. **5**, 10148 (2015).

[22] Y. F. Yu, Y. H. Fu, X. M. Zhang, A. Q. Liu, T. Bourouina, T. Mei, Z. X. Shen, and D. P. Tsai, Pure angular momentum generator using a ring resonator, Opt. Express **18**, 21651 (2010).

[23] X. Cai, J. Wang, M. J. Strain, B. Johnson-Morris, J. Zhu, M. Sorel, J. L. O'Brien, M. G. Thompson, and S. Yu, Integrated compact optical vortex beam emitters, Science **338**, 363 (2012).

[24] P. Miao, Z. Zhang, J. Sun, W. Walasik, S. Longhi, N. M. Litchinitser, and L. Feng, Orbital angular momentum microlaser, Science **353**, 464 (2016).

[25] J. B. Pendry, L. Martín-Moreno, and F. J. Garcia-Vidal, Mimicking surface plasmons with structured surfaces, Science **305**, 847 (2004).

[26] F. J. Garcia-Vidal, L. Martín-Moreno, and J. B. Pendry, Surfaces with holes in them: New plasmonic metamaterials, J. Opt. A: Pure Appl. Opt. **7**, S97 (2005).

[27] X. Shen, T. J. Cui, D. Martin-Cano, and F. J. Garcia-Vidal, Conformal surface plasmons propagating on ultrathin and flexible films, Proc. Natl. Acad. Sci. U.S.A. **110**, 40 (2013).

[28] H. Su, X. Shen, G. Su, L. Li, J. Ding, F. Liu, P. Zhan, Y. Liu, and Z. Wang, Efficient generation of microwave plasmonic vortices via a single deep-subwavelength meta-particle, Laser Photon. Rev. **12**, 1800010 (2018).

[29] J. Y. Yin, J. Ren, L. Zhang, H. Li, and T. J. Cui, Microwave vortex-beam emitter based on spoof surface plasmon polaritons, Laser Photon. Rev. **12**, 1600316 (2018).

[30] M. Wang, H. F. Ma, H. C. Zhang, W. X. Tang, X. R. Zhang, and T. J. Cui, Frequency-Fixed beam-scanning leaky-wave antenna using electronically controllable corrugated microstrip line, IEEE Trans. Antennas Propag. **66**, 4449 (2018).

[31] G. S. Kong, H. F. Ma, B. G. Cai, and T. J. Cui, Continuous leaky-wave scanning using periodically modulated spoof plasmonic waveguide, Sci. Rep. **6**, 29600 (2016).

[32] B. G. Cai, Y. B. Li, H. F. Ma, W. X. Jiang, Q. Cheng, and T. J. Cui, Leaky-Wave radiations by modulating surface impedance on subwavelength corrugated metal structures, Sci. Rep. **6**, 23974 (2016).

[33] C. A. Balanis, *Antenna Theory: Analysis and Design*, 3rd ed (John Wiley, Hoboken, NJ, 2005).

[34] A. B. Matsko and V. S. Ilchenko, Optical resonators with whispering-gallery modes-part I: Basics, IEEE J. Sel. Top. Quantum Electron. **12**, 3 (2006).

[35] Z. Bomzon, V. Kleiner, and E. Hasman, Pancharatnam–Berry phase in space-variant polarization-state manipulations with subwavelength gratings, Opt. Lett. **26**, 1424 (2001).

[36] A. Niv, G. Biener, V. Kleiner, and E. Hasman, Manipulation of the Pancharatnam phase in vectorial vortices, Opt. Express **14**, 4208 (2006).

[37] M. Guglielmi and D. R. Jackson, Broadside radiation from periodic leaky-wave antennas, IEEE Trans. Antennas Propag. **41**, 31 (1993).

[38] P. Burghignoli, G. Lovat, and D. R. Jackson, Analysis and optimization of leaky-wave radiation at broadside from a class of 1-D periodic structures, IEEE Trans. Antennas Propag. **54**, 2593 (2006).

[39] S. Paulotto, P. Baccarelli, F. Frezza, and D. R. Jackson, A novel technique for open-stopband suppression in 1-D periodic printed leaky-wave antennas, IEEE Trans. Antennas Propag. **57**, 1894 (2009).

[40] G. Lovat, P. Burghignoli, and D. R. Jackson, Fundamental properties and optimization of broadside radiation from uniform leaky-wave antennas, IEEE Trans. Antennas Propag. **54**, 1442 (2006).

[41] K. Cicek, Z. Hu, J. Zhu, L. Meriggi, S. Li, Z. Nong, S. Gao, N. Zhang, X. Wang, X. Cai, M. Sorel, and S. Yu, Integrated optical vortex beam receivers, Opt. Express **24**, 28529 (2016).

[42] S. A. Schulz, T. Machula, E. Karimi, and R. W. Boyd, Integrated multi vector vortex beam generator, Optics Express **21**, 16130 (2013).

[43] I. Moreno, J. A. Davis, I. Ruiz, and D. M. Cottrell, Decomposition of radially and azimuthally polarized beams using a circular-polarization and vortex-sensing diffraction grating, Optics Express **18**, 7173 (2010).